MATERIALS SCIENCE

Solution-processed transparent ferroelectric nylon thin films

Saleem Anwar[1,2], Daniel Pinkal[1], Wojciech Zajaczkowski[1], Philipp von Tiedemann[3,4], Hamed Sharifi Dehsari[1], Manasvi Kumar[1], Thomas Lenz[1], Ulrike Kemmer-Jonas[3], Wojciech Pisula[1,5], Manfred Wagner[1], Robert Graf[1], Holger Frey[3], Kamal Asadi[1]*

Ferroelectricity, a bistable ordering of electrical dipoles in a material, is widely used in sensors, actuators, non-linear optics, and data storage. Traditional ferroelectrics are ceramic based. Ferroelectric polymers are in-expensive lead-free materials that offer unique features such as the freedom of design enabled by chemistry, the facile solution-based low-temperature processing, and mechanical flexibility. Among engineering polymers, odd nylons are ferroelectric. Since the discovery of ferroelectricity in polymers, nearly half a century ago, a solution-processed ferroelectric nylon thin film has not been demonstrated because of the strong tendency of nylon chains to form hydrogen bonds. We show the solution processing of transparent ferroelectric thin film capacitors of odd nylons. The demonstration of ferroelectricity, as well as the way to obtain thin films, makes odd nylons attractive for applications in flexible devices, soft robotics, biomedical devices, and electronic textiles.

INTRODUCTION

Nearly three decades ago, it was found that the odd nylons show ferroelectric properties (1, 2). Nylons are made of repeating aliphatic units connected by amide functional groups. The letter n in n-nylon refers to the number of carbon atoms in a repeat unit. The amide groups have a large dipole moment of 3.7 D, and at the same time, they have a strong tendency to form hydrogen-bonded sheets (3). The crystalline structure, as well as ferroelectric properties, of nylons can be fine-tuned by varying the chemical structure, blending, and co-polymerization (4–6). Nylon-11, a chemical structure shown in the inset of Fig. 1A, is the most studied ferroelectric member of the family. Nylon-11 shows five crystalline phases: α, α′, γ, δ, and δ′ (7, 8). Ferro-electricity is only demonstrated for the δ′ phase, a poorly orga-nized hydrogen-bonded chain structure that enables the dipole (re)orientation and switching upon the application of an electric field (1, 9). The ferroelectric nylon-11 capacitors are fabricated by the uni-axial stretching of melt-quenched thick films, which yields free-standing foils with thickness of typically tens of micrometers.

The initial enthusiasm about ferroelectric odd nylons has come to a halt because of the inability to solution process ferroelectric thin films, as required for many of the envisioned microelectronic applications. Solution processing of nylon-11 thin films (and generally of all nylons) is a major challenge (10). Because of the strong hydrogen bond inter-action between the amide groups, nylons show insolubility in almost all common solvents. Nylons are soluble in (i) strong acids such as absolute H_2SO_4, which protonates the carbonyl bond and breaks the hydrogen bonding between the polymer chains and in (ii) highly polar solvents (11, 12), where hydrogen bonding is weakened because of the strong interaction between the amide groups and the polar sol-vent molecules. To realize solution-processed ferroelectric odd nylon thin films, two challenges should be addressed. First, both solvent types I and II are highly hygroscopic. During film formation processes such as spin coating, water, which is a nonsolvent for nylons, may condense into the drying film, causing vapor-induced phase separa-tion (VIPS), yielding a highly rough film with a cloudy appearance resulting in electrical shorts in capacitors (13, 14). Hence, VIPS should be effectively hindered during the process to yield smooth, pinhole-free thin films. Second, the ferroelectric δ′ phase has not been yet demon-strated using a solution processing technique. Therefore, the next chal-lenge is to enforce the crystallization of the odd nylon thin films into the ferroelectric δ′ phase upon solution processing. Processing the thin films from high boiling point solvents, e.g., m-cresol, typically leads to the α phase, whereas using low boiling point solvents, such as trifluoro-acetic acid (TFA), typically yields the γ phase (8). Both phases are not ferroelectric and therefore undesired. The realization of smooth, opti-cally transparent, pinhole-free solution-processed odd nylon thin films that are crystallized in the ferroelectric phase will be a major break-through in the field of ferroelectric polymers.

By revisiting the solution processing of nylons, we have tailored a solvent system with low vapor pressure, strong acidity, and strong hydrogen-bonding character. The solvent can dissolve all aliphatic nylons at room temperature through the formation of hydrogen bonds with the amide groups. The solvent mixture effectively dissolves all nylons, ranging from low odd–numbered nylons (in our case, nylon-5) to commercially available nylon-11. We introduce solution quench-ing to freeze odd nylons in the poorly organized hydrogen-bonded chain arrangement. Solution-quenched (SQ) thin films have been realized by spin coating of the odd nylon solution for a brief moment, followed by placement of the wet films in vacuum to deplete the sol-vent. The resulting SQ odd nylon thin films show a ferroelectric be-havior. We show that thin films are crystallized in the ferroelectric δ′ phase. We demonstrate the fabrication of extremely smooth and op-tically transparent films with high quality. The ferroelectric proper-ties of nylon-11 thin films are comparable to those of the thick films. We have compared the performance of nylon-11 ferroelectric capac-itor with those of the conventional ferroelectric polymers such as polyvinylidene difluoride (PVDF) and its random copolymer with trifluoroethylene [P(VDF-TrFE)]. Nylon-11 ferroelectric capacitors show superior performance under continuous stress cycles. The

[1]Max Planck Institute for Polymer Research, Ackermannweg 10, 55128 Mainz, Germany. [2]School of Chemical & Materials Engineering, National University of Sciences and Technology, Sector H-12, Islamabad, Pakistan. [3]Institute of Organic Chem-istry, Johannes Gutenberg University, Duesbergweg 10-14, Mainz, Germany. [4]Graduate School Materials Science in Mainz, Staudinger Weg 9, 55128 Mainz, Germany. [5]Department of Molecular Physics, Faculty of Chemistry, Lodz Univer-sity of Technology, Zeromskiego 116, 90-924 Lodz, Poland.
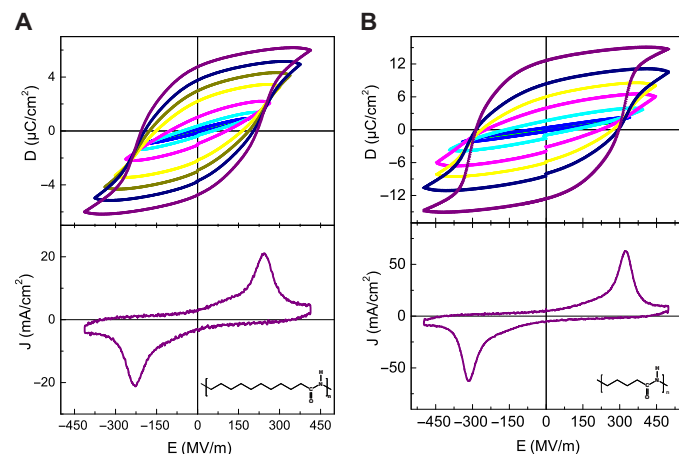*Corresponding author. Email: asadi@mpip-mainz.mpg.de

demonstration of solution-processed ferroelectric nylon thin films in combination with the simple synthesis and tunability of the chemical structure would potentially unlock the door to an unlimited number of hydrogen-bonded ferroelectric polymers.

RESULTS AND DISCUSSION

Ferroelectricity in SQ nylon thin films

The ferroelectric hysteresis loop of SQ nylon-11 thin films is shown in Fig. 1A. Thin films have been prepared by spin coating from 4 weight % solution of nylon-11 in TFA:acetone [60:40 mole percent (mol %)] solvent mixture, followed by immediate solvent quenching by placing the wet films in vacuum. For the field below 200 mega volts (MV)/m, the dielectric displacement, D, response is linear with respect to the applied electric field, E. Increasing the field beyond 200 MV/m opens hysteresis in the D-E loop. The loops are saturated when the field reaches 420 MV/m. The maximum remanent polarization, P_r, amounts to 4.7 μC/cm^2. As a benchmark measurement, we also determine P_r and coercive field, E_c, of 4.5 μC/cm^2 and 110 MV/m, respectively, for the melt-quenched-stretched (MQS) nylon-11 thick film as shown in fig. S1. The P_r values for SQ thin films agree well with those of MQS thick films and with those reported in the literature (1, 3, 9, 15). The E_c for SQ nylon-11 thin films amounts to 200 MV/m, which is higher than the benchmark value of MQS films (110 MV/m). We shall clarify this difference by the subtle difference in microstructure in the next section.

The ferroelectric loop of the SQ thin film of nylon-5 is given in Fig. 1B. Nylon-5 shows P_r = 12.5 μC/cm^2. Higher P_r values for nylon-5 are expected because the P_r for odd nylons increases linearly with the dipole density, i.e., 1.34×10^{-2} D/Å^3 as compared to 2.94×10^{-2} D/Å^3 for nylon-11 and nylon-5, respectively (4). Nylon-5 also exhibits higher E_c (300 MV/m). Notably, the D-E measurements have been performed repeatedly at fields exceeding 450 MV/m, and the capacitors have survived the test. Therefore, the breakdown field strength is well above 450 MV/m. Because of the larger number of hydrogen bonds per unit length, an increase in the E_c of nylon-5 is expected. Figure 1 is an unambiguous demonstration of solution-processed ferroelectric nylon thin films.
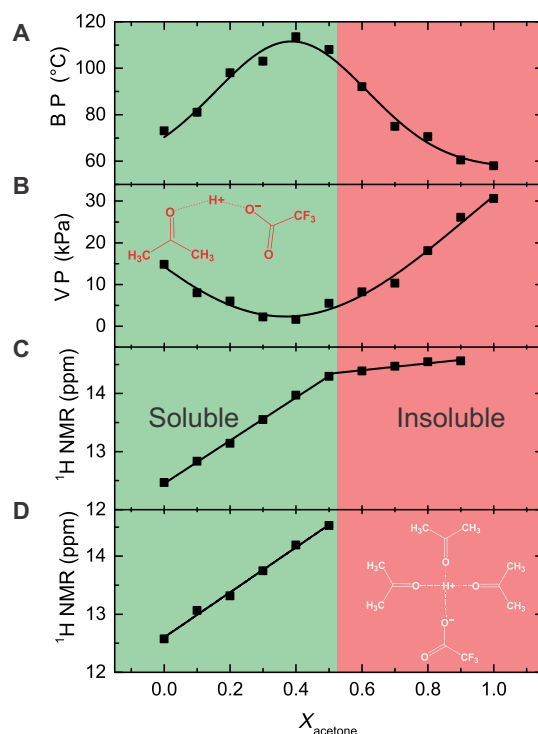
Solvent mixture of TFA:acetone

Nylon thin films processed from TFA-only solution (under exactly the same film formation conditions) do not show any ferroelectric behavior, in sharp contrast to TFA:acetone. Therefore, we set out to study the TFA:acetone solvent mixture.

The boiling point of TFA, as shown in Fig. 2A, substantially increases upon increasing acetone fraction. Conversely, the vapor pressure of the mixture decreases. The mixing of TFA with acetone is an exothermic process. At an intermediate composition of 40 mol % of acetone, the boiling point of the mixture is highest (i.e., 113°C) and the vapor pressure is lowest (i.e., 1.6 kPa) among all compositions. Upon further increase in the acetone mole fraction, the boiling point drops and the vapor pressure increases. TFA:acetone solvent mixture therefore shows negative deviation from Raoult's law.

For a deeper understanding, we have performed solution nuclear magnetic resonance (NMR). We use acetone-d_6 to monitor the proton shift of TFA. The solvent composition is changed from 100 mol % TFA to 100 mol % acetone-d_6. The mixture of TFA and acetone show additional carbonyl signals compared to the pure acetone-d_6 (fig. S2A). The additional signals are due to the exchange of hydrogen and deuterium, which can be easily explained with a keto-enol tautomerism (fig. S2B). The intermediate complex of TFA-H-acetone

Fig. 2. Dissolution mechanism of nylons in the TFA:acetone mixture. (A) Boiling point (B. P.) and **(B)** vapor pressure (V. P.) of the solvent mixture of TFA:acetone as a function of acetone mole fraction ($X_{acetone}$). The inset shows the schematic of the interactions between TFA and acetone molecules for 50:50 mol % TFA:acetone. **(C)** ^{1}H shift of the NMR (850.3 MHz at 298 K) spectra for different solvent mixtures of TFA:acetone-d_6 as a function of acetone mole fraction. **(D)** ^{1}H shift of the NMR (850.3 MHz at 298 K) spectra of nylon-11 solution for different solvent mixtures of TFA:acetone-d_6 as a function of acetone mole fraction. The solubility region for nylons is marked in green. The insolubility region due to the shielding of the proton is marked in red. The inset shows the schematic of the shielding of TFA by acetone molecules for 75:25 mol % TFA:acetone.

Fig. 1. Solution-processed ferroelectric nylon thin films. D-E hysteresis loop (top) and switching current (bottom) of **(A)** nylon-11 and **(B)** nylon-5, respectively. The insets show the respective chemical structures.

suggests that the acidic proton of TFA is shared with acetone molecules. Higher acidity of the solvent mixture is shown by the shift in proton spectra (fig. S3A). The positions of the ^{1}H chemical shifts are shown in Fig. 2C. TFA shows a proton peak at 12.47 parts per million (ppm). Upon the addition of acetone, the proton peak shifts linearly to a higher value of 14.30 ppm for 50:50 mol % TFA:acetone. The slope of the proton shift amounts to 3.7 ppm per mole fraction of acetone. For acetone between 60 and 90 mol %, the slope of the proton shift is much reduced to 0.6 ppm per mole fraction of acetone. We ascribe the proton shift to the formation of hydrogen bonds between TFA and acetone. For the individual components, the intermolecular hydrogen bonding is not present. In the mixture, however, strong hydrogen bonding is formed between carbonyl oxygen of acetone and H$^+$ of TFA. As a result, the tendency of the mixture molecules to go to vapor phase is reduced and the boiling point is increased. Moreover, the addition of acetone to the TFA leads to weaker binding of H$^+$ to TFA and eventually the deshielding of H$^+$. For 50:50 mol % TFA:acetone, the interaction schematics is shown in the inset of Fig. 2B, where the proton of TFA is shared between TFA and acetone. The hydrogen bonds between TFA and acetone have enthalpy of more than −10 kcal/mol and are among the strongest hydrogen bonds (16).

Acetone is not a solvent for nylons. In the next step, we perform the solubility test for nylon-11 in TFA:acetone mixtures. We find that a TFA:acetone mixture up to 50 mol % acetone dissolves nylons very well, whereas a 40:60 mol % TFA:acetone mixture does not dissolve nylons. The solubility region is marked in green in Fig. 2. The reason of insolubility of the nylon-11 at acetone concentration beyond 50 mol % is that the H$^+$ is covered with a sheath of acetone molecules. A schematic of 25:75 mol % TFA:acetone is shown in the inset of Fig. 2D. Because of the shielding of the H$^+$ by the acetone molecules, the proton cannot attack the hydrogen bonding between the bulky nylon chains, rendering nylons insoluble. We note that the same results are obtained for nylon-5.

To investigate the effect of the solvent mixture interaction with nylons, we monitor the acid proton shift for the nylon-11 solution in TFA:acetone. TFA shows a proton peak at 12.47 ppm (Fig. 2C). Nylon in TFA shifts the proton peak to 12.58 ppm (Fig. 2D). The shift indicates that the proton is shared between amide groups of nylon-11 and TFA. The addition of 10 mol % acetone, however, led to a stronger shift to 13.10 ppm, which increased linearly to 14.53 ppm at 50 mol %. The 50:50 mol % TFA:acetone is therefore the best solvent mixture to dissolve nylon-11. We have used the 60:40 mol % composition for solution processing of the films because of its highest boiling point and lowest vapor pressure. We note that diffusion order NMR (DOSY) (fig. S4) has shown no degradation of nylon-11 because of the increased acidity of TFA:acetone solvent mixture.

Microstructure study of the solution-processed thin films

We first study the surface topography of a conventionally spin-coated nylon-11 thin film, i.e., without SQ, from TFA:acetone solvent mixture. Because of the high boiling point of the solvent mixture and the strong interactions between TFA:acetone and nylon, the solvent evaporates very slowly from the film during the spin coating. Hence, spin coating times of nearly 4 min are required to obtain seemingly dry films with typical thickness of 500 nm. Respective atomic force microscopy (AFM) height image is shown in Fig. 3A. The topography shows the formation of a co-continuous coarse microstructure due to VIPS with a root mean square (RMS) roughness that amounts to 48 nm. These films do not show any ferroelectric behavior.

The AFM height topography of the SQ thin film (Fig. 3B) shows the formation of an extremely smooth surface. The application of vacuum quickly depletes the wet film from the solvent. VIPS is effectively hindered, and a very fine microstructure is obtained with an RMS roughness that amounts to only 4 nm.

To corroborate on the optical quality of the SQ thin film, we have measured the absorbance of the thin films as a function of wavelength, as shown in Fig. 3C. The SQ thin film shows interference fringes because of extreme film smoothness. For conventionally spin-coated films, the absorbance increases by two orders of magnitude without any interference patterns. The absorbance is fitted using the equation (17)

$$\alpha_{sc} = \frac{1}{d}\left(\frac{2\pi(n_f - n_a)\sigma_{RMS}}{\lambda}\right)^2 \qquad (1)$$

where d is the film thickness, n_f is the refractive index of nylon-11, which is 1.52 (18), n_a is the refractive index of ambient, σ_{RMS} is the roughness of the film, and λ is the wavelength of light.

The calculated σ_{RMS} from Eq. 1 for different film thicknesses is in good agreement with the experimental values of those obtained by AFM height topography (Fig. 3D). We note that the roughness for the SQ thin film remains well below 5 nm for different thicknesses. Furthermore, we have measured transparency and haze, as shown in fig. S5. The SQ thin film shows haze of only 0.3%, which is an order of magnitude lower than that of the conventionally spin-coated films.

Crystalline structure

We have determined the crystallinity from differential scanning calorimetry (DSC) (fig. S6). The SQ thin film and the benchmark MQS thick film show crystallinities of 25 and 26%, respectively. The SQ thin film shows crystallinity comparable to that of the MQS thick film. To gain insight into the crystalline structure of the nylon-11 SQ thin film, we have performed wide-angle x-ray diffraction (WAXD) and compared the results with WAXD diffractograms of the MQS thick film. The MQS film of nylon-11 has a polar δ′ phase, which is characterized by a metastable mesophase with randomly oriented hydrogen bonds along the backbone and between the adjacent chains (15, 19). The MQS film (Fig. 4A) shows a WAXD peak at 4.79 nm^{-1}, which corresponds to the low-angle (001) reflection of the δ′ phase, and is assigned to the smectic-like arrangement of the amide groups along the polymer chain with a d-spacing of 1.311 nm (3, 15, 20). The peak at 15.08 nm^{-1} is broad. To resolve the peak, we have performed WAXD along the parallel and perpendicular to the stretch direction (see fig. S8). The observed scattering angles for the (100) and (010) show only a small shift, meaning that (100) and (010) peaks are merged, and the peak value correspond to a d-spacing of 0.417 nm. The (100) and (010) peaks are assigned to the interchain distance along the hydrogen bonds and the intersheet distance between the hydrogen-bonded sheets, respectively (15, 20). We note that both reflections have almost identical position indicating low intermolecular order with hydrogen bonds that are randomly oriented along the backbone and between adjacent chains (3, 19).

Nylon-11 SQ thin films are readily crystalized in the ferroelectric δ′ phase. The WAXD pattern of the SQ film shows reflections similar to that of the δ′ phase MQS film. The (100)/(010) peak, however, shows broadening and a marginal shift in the position toward a higher q value of 15.30 nm^{-1} and a lower d-spacing of 0.411 nm. We have compared in table S1 the position of (100)/(010) and (001) peaks for all
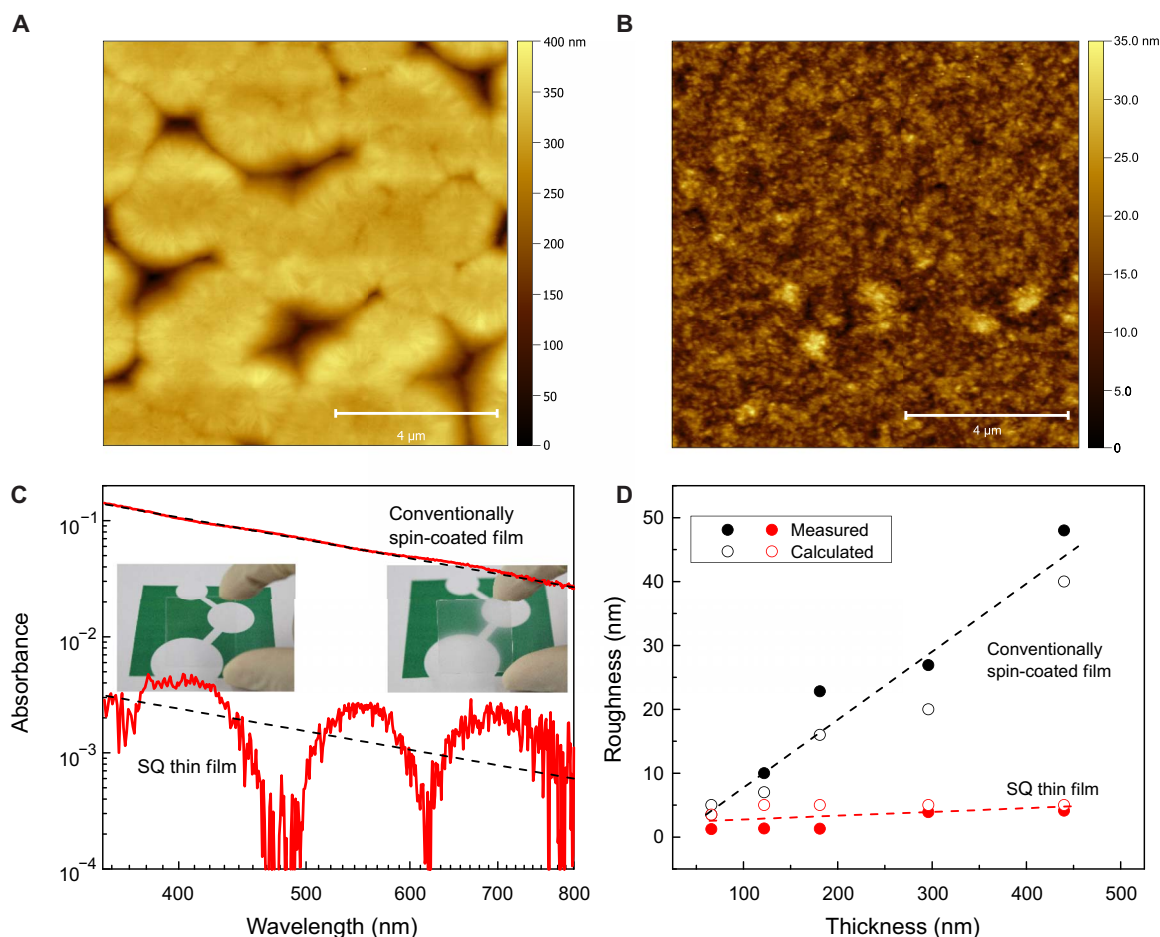
Fig. 3. Transparent solution-processed nylon-11 thin films. Tapping mode AFM height image of the (**A**) conventionally spin-coated and (**B**) SQ thin films. (**C**) Ultraviolet-visible absorption as a function of wavelength on a double logarithmic scale of the conventionally spin-coated thin film and the SQ thin film. The dashed lines are the calculated absorbance using Eq. 1. The inset shows optical quality of the SQ thin films; the images of the logo of the Max Planck Institute for Polymer Research are taken through the SQ thin film (left) and the conventionally spin-coated films (right). Photo credit: Saleem Anwar, Max Planck Institute for Polymer Research. (**D**) Evolution of the roughness of the conventionally spin-coated and the SQ thin film upon variation in thicknesses. The RMS roughness is measured by AFM height topography, while calculated roughness is determined using optical absorption measurement. The calculated roughness agrees well with the experimental roughness obtained by AFM. The dashed lines are guide to the eye.

different crystalline forms of nylon-11. The observed d-spacing for the (100)/(010) peak of the SQ thin film can be assigned to γ, γ′, or δ′ phase. However, the low-angle (001) reflection of the SQ film corresponds to a d-spacing of 1.311 nm and matches exactly with the one for the MQS film and the reported literature values for nylon-11 δ′ phase. The slight shift of the (100)/(010) peak for the SQ thin film is due to better intramolecular order, with hydrogen-bonded amide groups forming two-dimensional sheets (3). The ferroelectric switching in nylon-11 stems from the alignment of the intersheet hydrogen bonds. Lower intersheet spacing of the hydrogen bonds in the SQ thin film compared to the MQS film results in stronger intersheet dipolar interactions, and therefore, a larger E_c is required to switch the orientation of the dipoles in the SQ thin film. We note that a similar shift in coercive field to higher values has been reported for acid-treated nylon-11 MQS thick films (21, 22). On the basis of the WAXD, the nylon-11 SQ thin film is crystallized in the δ′ phase but with better order of the hydrogen-bonded amide dipoles.

To further corroborate on hydrogen bonding in SQ thin film, we have performed Fourier transform infrared (FTIR) spectroscopy and

solid-state NMR on both MQS film and SQ thin film. Full infrared (IR) scan for both films is shown in fig. S7. We focus on the hydrogen-bonded peaks, i.e., amide I and amide II, where amide I is attributed to the stretching of the C=O double bonds while amide II is due to the in-plane bending mode of N—H and the stretching mode of the central amide —N—CO— bond (20, 23, 24). Amide I and amide II peaks for MQS thick films occur at 1636 and 1544 cm^{-1}, respectively. The peaks for the SQ thin film, however, occur at slightly different wavenumbers (1634 and 1547 cm^{-1} for amide I and amide II, respectively). The position of the amide bands is sensitive to the details of the nylon chain packing and the interactions between the amide groups. It has been shown that, upon decreasing disorder, amide I and amide II bands shift to, respectively, lower and higher wavenumbers (25). The observed shifts of the amide I and amide II bands for the SQ thin film in comparison to the MQS film indicate the formation of more ordered hydrogen bonding in the SQ thin film, in agreement with WAXD data.

Final confirmation of better order in thin film comes from the solid-state NMR spectroscopy on the MQS film and the SQ thin film. ^{1}H
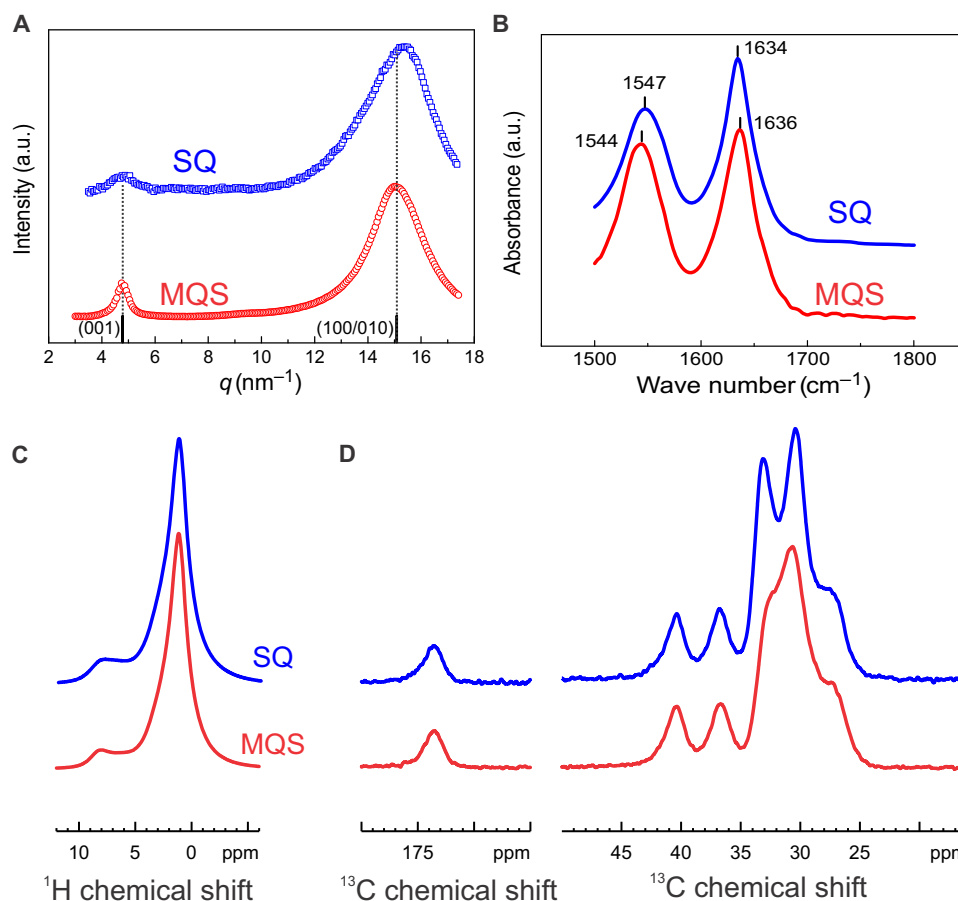
Fig. 4. Ferroelectric order in the SQ thin film of nylon-11. (**A**) WAXD patterns for the SQ thin film and the benchmark MQS film. The δ′ phase of nylon-11 has (001) peak at low q values and a broader peak at higher q values due to the superposition of (100)/(010) reflections. The solid lines show the deconvolution of the (100) and (010) reflections. The reported literature values for the δ′ phase are shown by black bars. (**B**) Room-temperature Fourier transform infrared (FTIR) spectra of the amide I and amide II bands for the SQ thin film and MQS film of nylon-11. (**C**) ^{1}H magic angle spinning (MAS) and (**D**) ^{13}C cross-polarization/MAS (CP/MAS) solid-state NMR spectra of the SQ thin film and MQS film. a.u., arbitrary units.

magic angle spinning (MAS) NMR spectra shown in Fig. 4C indicate an additional signal intensity of weakly hydrogen-bonded ^{1}H sites observed around 6 to 7 ppm in the SQ thin film, which is significantly weaker in the MQS film, in agreement with WAXD and FTIR spectroscopy. However, we observed more pronounced differences between the MQS film and the SQ thin film in the ^{13}C cross-polarization/MAS (CP-MAS) spectra shown in Fig. 4D. The ^{13}C CP/MAS NMR signals of carbonyl sites observed at 173.5 ppm and the two CH$_2$ units next to the hydrogen-bonding amide groups observed at 40.4 and 36.8 ppm match perfectly for the MQS film and the SQ thin film. For the aliphatic chain between the amide groups, however, we observed significant differences between the two films. The NMR signal of the aliphatic chains splits into two signals: the signal of the CH$_2$ segments in trans conformation at 33.0 ppm and the signal of the segments in gauche conformation at 30.4 ppm. In the MQS film, the CH$_2$ segments are predominantly in gauche conformation with only a minor trans contribution. In contrast, the trans-gauche distribution in the SQ thin film has a comparable population of both conformations. Taking into account that both films have a similar crystallinity and that CH$_2$ chains in noncrystalline regions will adopt preferably gauche conformations for entropic reasons, we conclude that aliphatic CH$_2$ chains in crystalline MQS nylon-11 adopt a crankshaft-like chain structure between neighboring amide units while

the prominent chain structure in the SQ nylon-11 thin film is significantly closer to the all-trans zigzag. The SQ thin film shows a strong conformational difference in comparison with the MQS film. The peak related to the trans conformation is much stronger, in perfect agreement with both WAXD and FTIR spectroscopy.
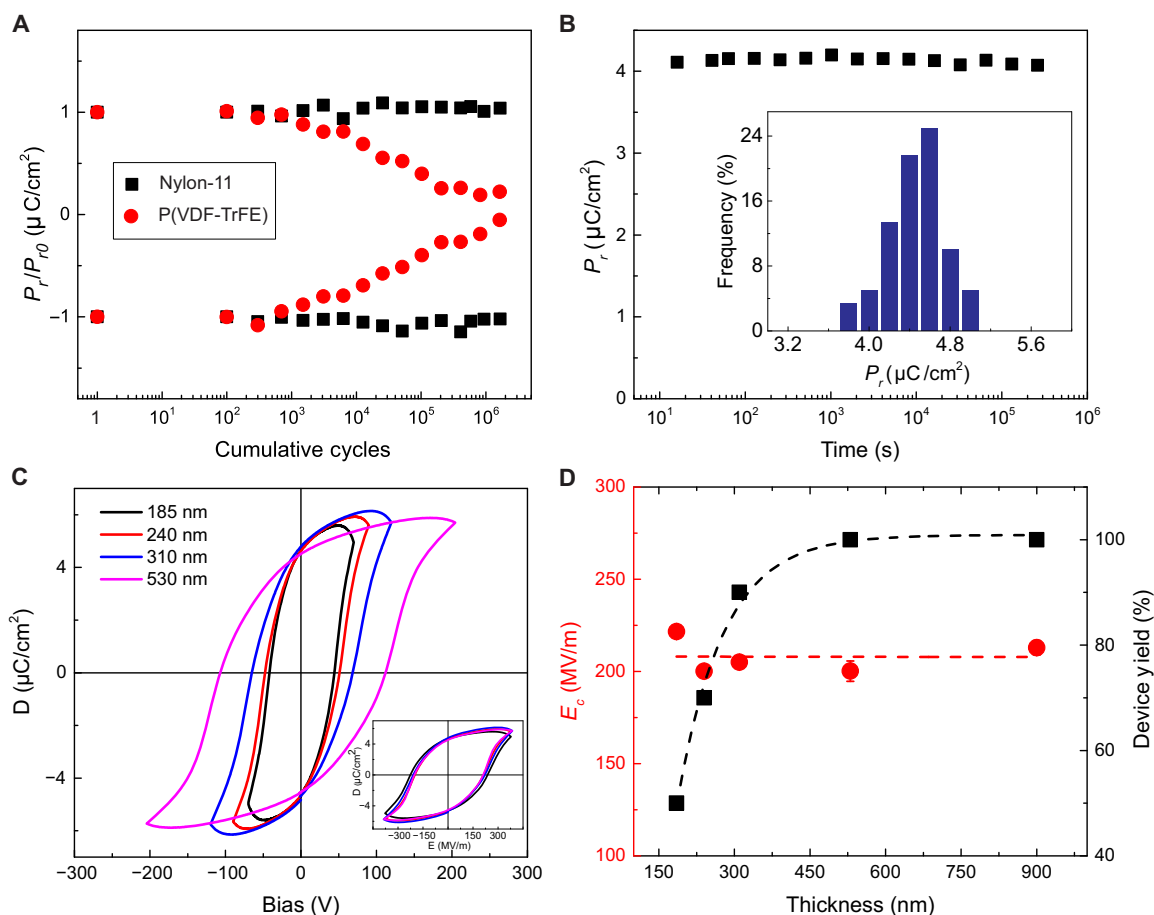
Ferroelectric capacitor performance

The destructive readout operation of a ferroelectric capacitor and the need for a field larger than E_c to reset data after each readout put a major demand on the stability of the polymer (polarization) upon repeated switching. P(VDF-TrFE) thin films, the workhorse of the ferroelectric polymers, typically show fatigue, i.e., decreased polarization as a function of repeated switching cycles (26). Fatigue depends on the amplitude, frequency, and profile of the driving electric field (27, 28). To benchmark the performance of the nylon ferroelectric capacitors, we have performed fatigue test and compared the results with those of P(VDF-TrFE) capacitors. The thicknesses of both nylon-11 and P(VDF-TrFE) thin films are about the same, and both capacitors have been stressed under identical conditions by the application of a switching field of $1.25 \times E_c$. The results of the fatigue tests are presented in Fig. 5A. The capacitors consisting of the SQ nylon-11 thin film exhibit a fatigue-free behavior for more than 10^6 write-erase cycles. In

contrast, P(VDF-TrFE) capacitors are highly prone to fatigue, with P_r starting to degrade at about 1000 cycles. We note that the fatigue behavior of P(VDF-TrFE) capacitors can be improved by using porous organic electrodes and by introducing a relaxing period between consecutive pulses (decreasing duty cycle) (29). Fatigue measurements on thin film ferroelectric capacitors from PVDF homopolymer are rare because of the difficulty to realize the ferroelectric phases in a thin film. To the best of our knowledge, polarization fatigue has been reported only for δ-PVDF thin film capacitors, where polarization reduces to 85% of its original value after 10^6 cycles, while SQ nylon-11 ferroelectric capacitors show superior fatigue behavior without any electrode modifications or decrease in the duty cycle. Table S2 provides a comparison between the ferroelectric performance of nylon-11 with PVDF and P(VDF-TrFE).

Retaining the polarization state is crucial for any application of the ferroelectric thin films. We have measured polarization retention time of the SQ nylon-11 ferroelectric capacitors, as shown in Fig. 5B. Polarization, measured at room temperature, was stable for a period longer than a week. We note that the scattering in P_r values obtained from different capacitors is very low. The inset of Fig. 5B shows the histogram for the P_r values from more than 80 nylon-11 ferroelectric thin film ca-

pacitors obtained by the SQ processing. The P_r shows a narrow distribution with a mean value of 4.5 ± 0.5 μC/cm².

Thickness scaling of the displacement versus voltage loops is presented in Fig. 5C for capacitors by varying the film thickness from 185 to 530 nm. All films show P_r of around 4.5 μC/cm². After normalizing all the loops for the electric field, as shown in the inset of Fig. 5C, all the hysteresis curves are overlaid, indicating that the E_c does not depend on layer thickness. The E_c obtained as a function of different layer thicknesses shows a plateau at 210 ± 10 MV/m, as presented in Fig. 5D. We note that all the processing steps have been conducted outside a clean room, where dust particles of the order of film thickness can lead to electrical shorts. Hence, the yield of functional capacitors with the SQ thin film thicknesses below 100 nm was 50%. The yield increases to 90% for films thicker than 300 nm. For thicknesses above 500 nm, the yield of nylon-11 ferroelectric capacitors is remarkably 100%. We note that, for every thickness, we have measured in excess of 70 capacitors. Nylon-11 thin films show a thickness variation of only 2% over the whole substrate. Thin films are free from pinholes, voids, and pores. Therefore, large area capacitors, with diameter of 10 mm, also show comparable performance.

Fig. 5. Performance of nylon-11 ferroelectric thin film capacitors. (**A**) $\pm P_r$ (normalized to their initial value) as a function of the cumulative number of cycles. Nylon-11 ferroelectric capacitors outperform P(VDF-TrFE). (**B**) Data retention as a function of time measured for a period longer than a week. The inset shows the histogram of the P_r values obtained for thin film (240 nm) capacitors from different fabrication batches. The SQ thin films show a narrow distribution in P_r. (**C**) D-E hysteresis loops for various film thicknesses as a function of applied bias and electric field (inset). (**D**) The evolution of E_c and the yield of functional ferroelectric capacitors with film thickness. The dashed lines are a guide to eye.

CONCLUSION

We have demonstrated solution-processed ferroelectric nylon thin film capacitors, where the ferroelectric δ′ phase has been obtained by solution quenching of the wet films still rich in solvent. The δ′ phase has been obtained from the mixture of 60:40 mol % TFA:acetone, where, because of the increased acidity, the solution mixture easily dissolves *n*-nylons. The solution mixture shows an increased boiling point and a decreased vapor pressure, which allow for solution processing of pinhole-free, ultrasmooth, and optically transparent nylon-11 thin films. The ferroelectric capacitors show fatigue-free behavior upon cycling. The simple synthesis and tunability of the chemical structure of nylons can now be fully exploited toward the optimization of the ferroelectric properties. The availability, ease of synthesis, and price advantage of nylons compared to ferroelectric fluoropolymers would allow upscaling of low-cost flexible thin films for the envisioned applications of ferroelectric polymers in microelectronics (30), memories (31, 32), and energy harvesting (33).

MATERIALS AND METHODS
Materials

Nylon-11 was purchased from Sigma-Aldrich. P(VDF-TrFE) (65 to 35) was purchased from Solvay. The weight-average molecular weight, M_w, of nylon-5, nylon-11, and P(VDF-TrFE) amounted to 5.8, 56, and 350 kg/mol, respectively. The number-average molecular weight, M_n, of nylon-5 was also determined on the basis of NMR end-group analysis in deuterated 1, 1, 1, 3, 3, 3-hexafluoro-2-propanol and amounted to 3.4 kg/mol. The molecular weight, M_n, of nylon-11 and P(VDF-TrFE) amounted to 39.7 and 170 kg/mol, respectively. TFA and acetone (99.8%, extra dry), were purchased from Carl Roth GmbH and Acros Organics, respectively. Cyclohexanone and acetone-d_6 (99.9 atom % D) were purchased from Sigma-Aldrich. Nylon-5 was synthesized from 2-piperidone via anionic ring-opening polymerization in bulk in the presence of 1 mol % N-acetyl-2-piperidone as starter and 10 mol % tetramethylammonium 2-oxopiperidin-1-ide following the work of Coutin and co-workers (25).

Nylon thin film preparation

Nylon solution was prepared by dissolving polymer in the TFA and acetone mixture (60:40 mol %). SQ thin films were fabricated by spin coating the solution on glass substrate, followed by solution quenching by applying high vacuum. The thickness of the films was controlled by changing the solution concentration. We also prepared MQS thick films by hot-pressing the nylon-11 pellets between two aluminum foils at 210 °C, followed by quenching in ice water. The films were uniaxially stretched at room temperature with a draw ratio of 3:1 at strain rate of 5 mm/min using a universal testing machine (ZwickRoell-Z005). The final thickness of MQS thick films was 15 to 20 μm.

P(VDF-TrFE) was dissolved in cyclohexanone. Thin films with thickness of typically 500 nm were prepared by spin coating.

Solution characterization

Absolute vapor pressure of solvent mixtures was measured using a home-built setup equipped with an electronic pressure sensor. A fixed volume of solvent was introduced in a sealed flask. The pressure at room temperature was measured after reaching the equilibrium. To measure the boiling point of the solvent mixture, a fine capillary tube sealed at one end was placed in the solvent mixture with the open-end downward into the liquid. A thermometer was attached with the test tube with a rubber band. The whole assembly was immersed in an oil bath. As the temperature was gradually increased, a quick evolution of bubbles started at the end of the capillary tube. Heating was continued for about 5 to 10 s more, and then, the heating source was removed. The temperature was recorded whenever the bubbles stopped coming out of capillary.

For solution NMR, the ^{1}H-NMR experiments were acquired with a 5-mm triple-resonance TXI ^{1}H/^{13}C/^{15}N probe equipped with a z-gradient on the 850.3-MHz Bruker AVANCE III System. The spectra were obtained with π/2-pulse lengths of 9 μs for proton (number of scans, 128; spectral width, 34,000 Hz) and 12 μs for carbon (scans, 2048; spectral width, 85,000 Hz) at 298 K and a relaxation delay time of 10 s each for ^{1}H-NMR and ^{13}C-NMR. The proton and carbon spectra were conducted in different mixtures of TFA and acetone-d_6, and the spectra were referenced with an external capillary—the residual C_2DHCl_4 at 5.93 ppm [δ(^{1}H)] and $C_2D_2Cl_4$ at 73.80 ppm [δ(^{13}C)]. The temperature was calibrated with a standard ^{1}H methanol NMR sample using the TopSpin 3.1 software (Bruker).

Microstructure investigation

AFM (NanoScope Dimension 3100, Bruker) was used to analyze the surface morphology of the thin films. Steady-state ultraviolet-visible absorption spectra were measured using a PerkinElmer Lambda 25 spectrophotometer. For haze measurement, we used a "Haze-gard plus" instrument (BYK-Gardner GmbH, Germany) for macroscopic optical properties using white light. Haze is defined as the part of light that deviates from the directly transmitted light at an angle higher than 2.5°. The thickness of the films was measured with a surface profilometer. DSC (DSC3+, METTLER TOLEDO) was performed under N_2 atmosphere at a scan rate of 10°C/min. WAXD measurements of the films were performed at the DELTA Synchrotron using beamline BL09 with a photon energy of 13 keV (λ = 0.9537 Å). The beam size was 1.0 mm by 0.2 mm (width by height), and samples were irradiated just below the critical angle for total reflection with respect to the incoming x-ray beam (~0.1°). The diffracting intensity was detected on a two-dimensional image plate (MAR-345) with a pixel size of 150 μm (2300 by 2300 pixels), and the detector was placed 523 mm from the sample center. Diffraction data are expressed as a function of the diffraction vector: $q = 4\pi/\lambda \sin(\Theta)$, where Θ is a half the diffraction angle and λ = 0.9537 Å is the wavelength of the incident radiation. Here, q_{xy} (q_z) is a component of the diffraction vector in plane (out-of-plane) to the sample surface. All x-ray measurements were performed under vacuum (~1 mbar) to reduce air scattering and beam damage to the sample. All WAXD data processing and analysis were performed by using the software package Datasqueeze (www.physics.upenn.edu/~heiney/datasqueeze/index.html). The IR spectra of nylon-11 films were recorded at room temperature using a Tensor II FTIR spectrometer with a resolution of 4 cm^{-1}.

Solid-state NMR measurements were performed with a 2.5-mm ^{1}H/X double-resonance CP/MAS probe at a Bruker 700 MHz AVANCE III NMR system. All measurements were taken at MAS speeds of 25 kHz. CP/MAS measurements were acquired with a contact time of 1 ms and 100-kHz radio frequency nutation frequency swept-frequency two-pulse phase modulation high-power composite pulse decoupling. Chemical shifts were referenced to tetramethylsilane using the CH_3 group of L-alanine with the ^{1}H peak at 1.3 ppm and the ^{13}C peak at 20.5 ppm as a secondary standard.

Capacitor fabrication

The capacitors were fabricated on a glass substrate on which 50-nm-thick Au bottom electrodes with a 1-nm Cr adhesion layer were thermally evaporated using a shadow mask. After deposition of thin film, gold top electrodes (50 nm) were deposited using shadow mask to form a crossbar pattern with the device area of 0.0016 cm^2. For the free-standing MQS thick film, capacitors were fabricated by thermal evaporation of gold (50 nm) on both sides with the device area of 0.74 cm^2.

Ferroelectric characterization

Ferroelectric capacitors were characterized in a probe station in a vacuum of 10^{-5} mbar. D-E hysteresis loops were measured using a Radiant precision multiferroic test system (Radiant Technologies Inc.) equipped with a high-voltage amplifier. Data retention and polarization fatigue were measured using the same setup. The fatigue test was performed using a continuous triangular waveform with the amplitude of $1.25 \times E_c$, respectively, 250 and 75 MV/m at 100 Hz for nylon-11 and P(VDF-TrFE). After a predefined number of cycles, the remanent polarization was determined by PUND (positive up negative down) measurement using 10-ms-wide pulses. For data retention, a write pulse is followed by two read pulses of the same amplitude but opposite direction. All pulse widths were fixed at 10 ms.

Ferroelectricity in MQS thick films

A bipolar triangular waveform at 10 Hz was applied at room temperature to the samples to study the D-E hysteresis loop. As can be seen from fig. S1, when the poling field is below 180 MV/m, a linear dielectric loop is observed for all samples as the field was too low for the dipoles to switch. But when the field was increased to 200 to 250 MV/m, a clear ferroelectric hysteresis loop was observed. The figure below the D-E loop shows the current density curve. The values of P_r and E_c are in good agreement with the literature values (3, 15).

Solution NMR

Carbon measurements of the mixture show some additional carbonyl signals compared to pure acetone-d_6. For example, in the mixture 80:20 mol % acetone-d_6:TFA, at least six different signals are detected, with a chemical shift difference of 0.06 ppm (60 parts per billion), which is typical for carbon shift when exchanging a deuterium with a proton next a carbonyl group (CD$_3$C=O to CD$_2$HC=O) (fig. S2A). The exchange of hydrogen and deuterium can be easily explained via the keto-enol tautomerism, in which all deuterium in acetone-d_6 can be substituted with the protons coming from TFA (fig. S2B). The ^{1}H spectra of solution NMR of TFA:acetone mixtures are shown in fig. S3. Figure S4 shows the NMR DOSY measurements for nylon-11 solution in pure TFA and TFA:acetone. The two different diffusion measurements show no change in the diffusion coefficient of the nylon-11 to corroborate that there is no change in the molecular size of the polymer using the TFA:acetone mixture.

Haze measurement

To show the optical quality of the films, we performed haze measurements, as shown in fig. S5 for different film thicknesses. Haze is due to internal or surface scattering due to particles/defects trapped within the film or roughness of the film, respectively (13). The value of haze for the conventionally spin-coated thin film for all thicknesses from 300 nm is 4% and linearly increases to 42% for 900-nm thin films. The SQ thin films however showed substantially lower haze values ranging from 0.3 for 300 nm to 4% for 900-nm thin films. By using solution quenching and high evaporation rate of solvent, thin films of high optical qualities were obtained.

Differential scanning calorimetry

The first heating cycle for the nylon-11 SQ thin film and MQS film is shown in fig. S6. After subtracting heat of cold crystallization from heat of melting, the degree of crystallinity (χ_c) was determined using heat of fusion of 100% crystalline nylon-11, which is 225 (J/g) (15). A decrease of 4°C in melting point of the SQ thin film was observed as the film was processed from solution (20).

Fourier transform infrared spectroscopy

Figure S7 shows the FTIR spectra of the nylon-11 SQ thin film and MQS film measured at room temperature. The spectra are normalized to 2852 cm^{-1}, the absorption band of symmetric CH$_2$ stretching (3). The spectra for the SQ thin film were shifted vertically for clarity. The regions 500 to 800 cm^{-1} consist of the amide VI and V bands and appeared at 586 and 690 cm^{-1} for the SQ thin film, respectively. Comparing peaks with the MQS film gives an indication of the same phase (δ′) in both the MQS film and the SQ thin film. The progression bands from the methylene sequence appeared from 1100 to 1400 cm^{-1}, showing no periodic change in the intensities of all films. A shoulder at 1420 cm^{-1} (CH$_2$ scissoring band) for both films shows same conformations in C—C bond near CO-vicinal CH$_2$ group (24). The hydrogen-bonded N—H stretching was observed at 3292 cm^{-1} for both the SQ thin film and the MQS film.

Wide-angle x-ray diffraction

WAXD measurements were performed both along the parallel and perpendicular to the stretch direction for the MQS film to better resolve the 100 and 010 peaks. The resulting diffractograms are given in fig. S8 and show resolving of the peak at ~15 nm^{-1} to two closely spaced peaks. The best fit to the WAXD pattern, as discussed in the main text, was obtained when we placed the peak position of the (100) and (010) reflections at d-spacing of 0.416 and 0.417 nm, respectively.

REFERENCES AND NOTES

1. J. W. Lee, Y. Takase, B. A. Newman, J. I. Scheinbeim, Ferroelectric polarization switching in Nylon-11. *J. Polym. Sci. B* **29**, 273–277 (1991).

2. Y. Takase, J. W. Lee, J. I. Scheinbeim, B. A. Newman, High-temperature characteristics of Nylon-11 and Nylon-7 piezoelectrics. *Macromolecules* **24**, 6644–6652 (1991).

3. Z. Zhang, M. H. Litt, L. Zhu, Understanding the paraelectric double hysteresis loop behavior in mesomorphic even-numbered nylons at high temperatures. *Macromolecules* **50**, 5816–5829 (2017).

4. B. Z. Mei, J. I. Scheinbeim, B. A. Newman, The ferroelectric behavior of odd-numbered nylons. *Ferroelectrics* **144**, 51–60 (1993).

5. L. Telen, P. Van Puyvelde, B. Goderis, Random copolymers from polyamide 11 and polyamide 12 by reactive extrusion: Synthesis, eutectic phase behavior, and polymorphism. *Macromolecules* **49**, 876–890 (2016).

6. Z. Zhang, M. H. Litt, L. Zhu, Achieving relaxor ferroelectric-like behavior in nylon random copolymers and terpolymers. *Macromolecules* **50**, 9360–9372 (2017).

7. J. Pepin, V. Miri, J.-M. Lefebvre, New insights into the Brill transition in polyamide 11 and polyamide 6. *Macromolecules* **49**, 564–573 (2016).

8. H. S. Nalwa, *Ferroelectric Polymers: Chemistry: Physics, and Applications* (CRC Press, 1995).

9. S. Ikeda, T. Saito, M. Nonomura, T. Koda, Ferroelectric properties and polarization reversal phenomena in nylon 11. *Ferroelectrics* **171**, 329–338 (1995).

10. E. L. Papadopoulou, F. Pignatelli, S. Marras, L. Marini, A. Davis, A. Athanassiou, I. S. Bayer, Nylon 6, 6/graphene nanoplatelet composite films obtained from a new solvent. *RSC Adv.* **6**, 6823–6831 (2016).

11. J. R. Schaefgen, C. F. Trivisonno, Polyelectrolyte behavior of polyamides. I. Viscosities of solutions of linear polyamides in formic acid and in sulfuric acid. *J. Am. Chem. Soc.* **73**, 4580–4585 (1951).

12. N. Tsutsumi, T. Yamaoka, Ferroelectric properties of ultrathin films of Nylon 11. *Thin Solid Films* **518**, 814–818 (2009).

13. M. Li, I. Katsouras, C. Piliego, G. Glasser, I. Lieberwirth, P. W. M. Blom, D. M. de Leeuw, Controlling the microstructure of poly(vinylidene-fluoride) (PVDF) thin films for microelectronics. *J. Mater. Chem C Mater.* **1**, 7695–7702 (2013).

14. H. S. Dehsari, J. J. Michels, K. Asadi, Processing of ferroelectric polymers for microelectronics: From morphological analysis to functional devices. *J. Mater. Chem. C Mater* **5**, 10490–10497 (2017).

15. Z. Zhang, M. H. Litt, L. Zhu, Unified understanding of ferroelectricity in *n*-nylons: Is the polar crystalline structure a prerequisite? *Macromolecules* **49**, 3070–3082 (2016).

16. R. E. Lundin, F. E. Harris, L. K. Nash, The vapor phase association of trifluoroacetic acid. *J. Am. Chem. Soc.* **74**, 4654–4656 (1952).

17. A. Poruba, A. Fejfar, Z. Remeš, J. Špringer, M. Vaněček, J. Kočka, J. Meier, P. Torres, A. Shah, Optical absorption and light scattering in microcrystalline silicon thin films and solar cells. *J. Appl. Phys.* **88**, 148–160 (2000).

18. W. J. Roff, J. R. Scott, *Fibres, films, plastics and rubbers: A handbook of common polymers* (Elsevier, 2013).

19. V. Gelfandbein, D. Katz, Pyroelectric response and crystal structure of Nylon 11. *Ferroelectrics* **33**, 111–117 (2011).

20. S. S. Nair, C. Ramesh, K. Tashiro, Crystalline phases in nylon-11: studies using HTWAXS and HTFTIR. *Macromolecules* **39**, 2841–2848 (2006).

21. E. Balizer, J. Fedderly, D. Haught, B. Dickens, A. S. DeReggi, in *1991 Conference on Electrical Insulation and Dielectric Phenomena (CEIDP'91)*, Annual Report (IEEE, 1991), pp. 193–200.

22. E. Balizer, J. Fedderly, D. Haught, B. Dickens, A. S. Dereggi, FTIR and x-ray study of polymorphs of Nylon 11 and relation to ferroelectricity. *J. Polym. Sci. B* **32**, 365–369 (1994).

23. D. J. Skrovanek, P. C. Painter, M. M. Coleman, Hydrogen bonding in polymers. 2. Infrared temperature studies of nylon 11. *Macromolecules* **19**, 699–705 (1986).

24. H. Isoda, Y. Furukawa, Electric-field-induced dynamics of polymer chains in a ferroelectric melt-quenched cold-drawn film of Nylon-11 using infrared spectroscopy. *J. Phys. Chem. B* **119**, 14309–14314 (2015).

25. S. M. Aharoni, *n-Nylons, their Synthesis, Structure, and Properties* (J. Wiley & Sons, 1997).

26. C. J. Lou, Polarization fatigue in ferroelectric thin films and related materials. *J. Appl. Phys.* **105**, 024101 (2009).

27. G. Zhu, Z. Zeng, L. Zhang, X. Yan, Polarization fatigue in ferroelectric vinylidene fluoride and trifluoroethylene copolymer films. *Appl. Phys. Lett.* **89**, 102905 (2006).

28. X. Zhang, H. Xu, Y. Zhang, Temperature dependence of coercive field and fatigue in poly(vinylidene fluoride-trifluoroethylene) copolymer ultra-thin films. *J. Phys. D Appl. Phys.* **44**, 155501 (2011).

29. D. Zhao, I. Katsouras, M. Li, K. Asadi, J. Tsurumi, G. Glasser, J. Takeya, P. W. M. Blom, D. M. de Leeuw, Polarization fatigue of organic ferroelectric capacitors. *Sci. Rep.* **4**, 5075 (2014).

30. R. C. G. Naber, K. Asadi, P. W. M. Blom, D. M. de Leeuw, B. de Boer, Organic nonvolatile memory devices based on ferroelectricity. *Adv. Mater.* **22**, 933–945 (2010).

31. M. Kumar, H. Sharifi Dehsari, S. Anwar, K. Asadi, Air-stable memory array of bistable rectifying diodes based on ferroelectric-semiconductor polymer blends. *Appl. Phys. Lett.* **112**, 123302 (2018).

32. H. Sharifi Dehsari, M. Kumar, A. Saad, M. Hassanpour Amiri, C. Yan, S. Anwar, G. Glasser, K. Asadi, Thin-film polymer nanocomposites for multiferroic applications. *ACS Appl. Nano Mater.* **1**, 6247–6257 (2018).

33. Q. Jing, S. Kar-Narayan, Nanostructured polymer-based piezoelectric and triboelectric materials and devices for energy harvesting applications. *J. Phys. D Appl. Phys.* **51**, 303001 (2018).

34. M. Li, H. J. Wondergem, M.-J. Spijkman, K. Asadi, I. Katsouras, P. W. M. Blom, D. M. de Leeuw, Revisiting the δ-phase of poly(vinylidene fluoride) for solution-processed ferroelectric thin films. *Nat. Mater.* **12**, 433–438 (2013).

35. R. G. Kepler, R. A. Anderson, Piezoelectricity in polymers. *Crit. Rev. Solid State Mater. Sci.* **9**, 399–447 (2006).

36. T. Lenz, H. Sharifi Dehsari, K. Asadi, P. W. M. Blom, W. A. Groen, D. M. de Leeuw, Thin film thermistor with positive temperature coefficient of resistance based on phase separated blends of ferroelectric and semiconducting polymers. *Appl. Phys. Lett.* **109**, 133302 (2016).

37. S. Z. Yuan, X. J. Meng, J. L. Sun, Y. F. Cui, J. L. Wang, L. Tian, J. H. Chu, Abnormal polarization enhancement effects of P(VDF-TrFE) films during fatigue process. *Phys. Lett. A* **375**, 1612–1614 (2011).

38. Q. Zhang, Z. Mo, H. Zhang, S. Liu, S. Z. D. Cheng, Crystal transitions of Nylon 11 under drawing and annealing. *Polymer* **42**, 5543–5547 (2001).

39. J. O. Fernandez, G. M. Swallowe, S. F. Lee, Crystallization of Nylon 11 under compressive high strain rates. *J. Appl. Polym. Sci.* **80**, 2031–2038 (2001).

40. G. Wu, O. Yano, T. Soen, Dielectric and piezoelectric properties of nylon 9 and nylon 11. *Polym. J.* **18**, 51–61 (1986).

41. K. G. Kim, B. A. Newman, J. I. Scheinbeim, Temperature dependence of the crystal structures of nylon 11. *J. Polym. Sci. Pt. B Polym. Phys.* **23**, 2477–2482 (1985).

42. B. A. Newman, P. Chen, K. D. Pae, J. I. Scheinbeim, Piezoelectricity in nylon 11. *J. Appl. Phys.* **51**, 5161–5164 (1980).

43. J. W. Lee, Y. Takase, B. A. Newman, J. I. Scheinbeim, Effect of annealing on the ferroelectric behavior of nylon-11 and nylon-7. *J. Polym. Sci. Pt. B Polym. Phys.* **29**, 279–286 (1991).

44. L. Chocinski-Arnault, V. Gaudefroy, J. L. Gacougnolle, A. Riviere, Memory effect and crystalline structure in polyamide 11. *J. Macromol. Sci. Pt. B Phys.* **41**, 777–785 (2007).

Citation: S. Anwar, D. Pinkal, W. Zajaczkowski, P. von Tiedemann, H. Sharifi Dehsari, M. Kumar, T. Lenz, U. Kemmer-Jonas, W. Pisula, M. Wagner, R. Graf, H. Frey, K. Asadi, Solution-processed transparent ferroelectric nylon thin films. *Sci. Adv.* **5**, eaav3489 (2019).